Computational Materials Science 218 (2023) 111973

Contents lists available at ScienceDirect

Computational Materials Science

journal homepage: www.elsevier.com/locate/commatsci

Full Length Article

Characterization of graphene reinforced 3C-SiC composite as a metal-free friction material using molecular dynamics simulation

Yizhan Zhang *, Kingsford Koranteng, Yun-Bo Yi

Department of Mechanical and Materials Engineering, University of Denver, Denver, CO, USA

ARTICLE INFO

Keywords:
Molecular dynamics
Metal-free friction material
Graphene/3C-SiC nanocomposite
Tribological properties

ABSTRACT

In this work, the tribological, mechanical and thermal properties of graphene (Gr)-based 3C-SiC nanocomposite as a metal-free friction material were first studied by using molecular dynamics (MD) simulations. In tribological properties, the frictional force, normal force, effective coefficient of friction and wear rate were investigated. The effects of scratching depth, temperature, scratching velocity and the number of Gr layers in the composite to the friction process were considered. Young's modulus, ultimate tensile stress (UTS) and failure strain in the mechanical properties, and thermal conductivity in the thermal property were also included to understand the tribological performances of the composite. The interfacial interaction energy was evaluated to characterize the effect of interface on material properties. The validations were performed on some representative results. In the simulation results with the selected configurations which are listed in the subsequent content, the nanocomposite showed the lowest wear rate with an appreciable coefficient of friction at the scratching depth of 10 Å. 10 m/s was the optimal scratching speed to maintain the best wear performance. A temperature of 300 K yielded the highest coefficient of friction and the lowest wear rate. The model with three Gr layers showed a relatively high coefficient of friction and a relatively low wear rate. The model with five Gr layers stacked in 3C-SiC exhibited the best mechanical performance. The nanowire model with two Gr layers showed a higher thermal conductivity. The research findings will provide guidance in design and manufacturing of Gr/3C-SiC friction materials. The study will also help understand the effect of Gr as a potential reinforcement for metal-free friction materials.

1. Introduction

The friction materials used for brake systems are very important in many areas such as the automotive and aerospace industries. Traditionally, brake pads and discs are made of metals or alloys because of their superior thermal properties. They have the ability to withstand and dissipate heat quickly in brake systems. Besides, their high strength and modulus create high resistance to large pressure and friction. However, due to the negative impact of metal ingredients on the environment, semi-metallic friction materials have been widely used. Meanwhile, the use of semi-metallic material does not adequately minimize the effect of metals on the environment. This has prompted researchers to switch to environmentally friendly, metal-free compositions in brake pad and clutch applications. However, the absence of metal compositions can make the friction material more susceptible to heat, leading to short service life of the friction materials. In an automotive brake system, there is a common phenomenon called thermal–mechanical instabilities (TMI), which may cover thermal-elastic instabilities (TEI), thermal buckling, dynamic instabilities as well as their couplings. The phenomenon can generate hot spots and excessive thermal stresses to cause structural instability, resulting in acceleration of material failure. In order to extend the service life while maintaining the effective performance of metal-free friction material, a good thermal stability, high strength and high wear resistance will be necessary.

A significant amount of prior studies on metal-free friction materials have been. As a typical non-metal friction material, SiC has been proven to possess high thermal stability and hardness with excellent tribological performance [1]. Zhou et al. performed an experiment to investigate the tribological properties of SiC and the effect of the addition of graphite on the micro scale [2]. Liu et al. added nano-SiO2 in NBR through MD and found that nano-SiO2 can reduce the possibility of collision and the temperature at the friction interface, which then reduces the interfacial friction stress and the potential wear of NBR [3].

More importantly, Gr can also be a useful reinforcement material due to its excellent mechanical properties and thermal properties [4–6], and therefore Gr has a huge prospect in the automotive industry [7].

---

* Corresponding author.
E-mail addresses: Yizhan.Zhang@du.edu (Y. Zhang), Koranteng@du.edu (K. Koranteng), Yun-Bo.Yi@du.edu (Y.-B. Yi).

https://doi.org/10.1016/j.commatsci.2022.111973
Received 9 July 2022; Received in revised form 6 December 2022; Accepted 8 December 2022

Although the Gr industry is still in the early stages with many challenges to its applications, a substantial progress has been made with regard to its mass production in the industry [8]. There are many works related to the MD simulation for the mechanical properties of Gr/SiC composite in the literature [9–11], and some researchers have also studied the thermal conductance between SiC and Gr [12–14]. For example, Llorente et al. [15] investigated the tribological performance of Gr/SiC composites under dry sliding in the laboratory and found that the wear resistance of SiC was improved significantly by creating a wear protecting Gr-based tribo-film from the Gr fillers. However, the friction simulation of Gr/SiC nanocomposite using MD has not been discussed in depth. 3C-SiC, also called β-SiC, is one of the SiC polytypes with zinc blende cubic crystal structure. Because of its low thermal expansion, excellent corrosion resistance, relatively high modulus, good resistance to high temperature and high pressure [16], 3C-SiC is a promising material for metal-free friction material. In addition, Gr has fascinating mechanical and thermal properties such as high Young's modulus, thermal conductivity, flexibility and hardness, and therefore Gr is also a superior reinforcement material [17]. In general, Gr can interact with SiC surfaces by either Van der Waals (VdWs) force or covalent bonds [18]. The strong bonding between SiC and Gr is of interest in recent years because it responds differently from the ones with weak interactions. However, it remains a challenge to produce covalently bonded interactions between SiC and Gr in manufacturing. Some common methods to prepare the covalently bonded Gr/SiC composite are through epitaxial growth [18] or microwave plasma chemical vapor deposition (CVD) [19]. There is also a new technology of synthesizing Gr/SiC composites, which is helicon wave plasma CVD invented by Chen et al [20]. Filleter et al. [21] used a method called thermal decomposition synthesis to grow single and bilayer Gr films on the Si-terminated (0001). They showed that the underlying interface layer has a very similar structure to Gr, and the transition from atomic stick–slip friction to a regime of ultralow friction with certain normal load and tip-sample interaction potential. In this research, a Gr/3C-SiC nanocomposite model with covalent bonds in-between is constructed by using non-reactive classical MD simulation at the nanoscale to evaluate its potential use as friction material and provide data on finding good candidates for making metal-free friction materials. The structure of the nanocomposite is basically a laminate with two to four Gr sheets stacking separately in the bulk 3C-SiC. The laminate structure, which usually has a high strength-to-weight ratio [22], may improve the strength, stability, and other properties. A compressed Gr laminate could also have a higher thermal conductivity [23]. Moreover, it was reported that forming the covalent bonds between Gr flakes could considerably enhance the thermal conductivity of laminates [24]. In this work, coefficient of friction, wear behavior, Young's modulus, tensile strength, and thermal conductivity of the covalent bonding Gr/3C-SiC nanocomposite laminate under various circumstances were studied for the first time. The spatial von-Mises stress distribution and temperature distribution of the workpiece in a scratching simulation were discussed. The effect of the scratching depth, scratching speed, temperature, internal stress, number of Gr layers on the tribological performance, the effect of the number of Gr layers on the mechanical performance, and effect of the length of the model, the number of Gr layers on the thermal conductivity of the Gr/3C-SiC nanocomposite laminate were the main objective to study in this work. We believe the present work will be valuable in studying the potential use of covalent bonding Gr/3C-SiC composite laminate in practical applications related to the automotive industry by providing in-depth knowledge and guidance for the use of metal-free friction materials.

2. Simulation models and methods

2.1. Tribological properties of Gr/3C-SiC nanocomposite

In the evaluation of tribological properties, a block Gr/3C-SiC nanocomposite laminate model is developed with a spherical diamond tool scratching on the surface of the laminate. The spherical diamond tool has the tendency to deform any material softer than it while imitating the asperity on the friction surface at the nanoscale. Basically, there are three different scenarios corresponding to the number of Gr in the model with a single layer, two layers, and three layers within the body of SiC, respectively. One of the schematics of the model is shown in Fig. 1.

The workpiece with the dimension of 240 × 150 × 77 (units: Å) contains a stack of armchair Gr layers within 3C-SiC bulk matrix. The distance between adjacent Gr layers is about 17 Å. In Fig. 1, the Si atoms in the main laminate body are in yellow, the C atoms are in gray, and the Gr atoms are in purple. Below the main body, there are two additional SiC layers. One is 7 Å in height with dark blue Si atoms and light green C atoms as the thermostat layer to simulate the heat dissipation process during friction. The other one is 5 Å in height with red Si atoms and light blue C atoms as the boundary layer to be immobilized to avoid the movement of the workpiece during friction [25]. The hard spherical indenter with a radius of 50 Å is in diamond structures with the C atoms in dark green. In the laminate model, the interactions between SiC and Gr are set as covalent bonding. Moreover, to avoid the effect from the different interfaces between the two phases on the material's properties, the surfaces of SiC in direct contact with Gr layers are all Si-terminated. In this system, three types of potentials are used. Tersoff [26] potential is implemented to describe the interactions inside SiC and the interactions between SiC and Gr. Since the Gr layers are fully connected with SiC by covalent bonds, there are no VdWs interactions between Gr layers; Adaptive Intermolecular Reactive Empirical Bond Order (AIREBO) potential [27] with a cut-off distance of 2 Å [28] is utilized for the interactions in Gr layer; The last one is Morse potential with a cut-off distance of 10 Å to represent the interactions between the indenter and the workpiece [29]. Here, Tersoff potential computes the potential energy of a system of atoms in three-body interactions. AIREBO potential is developed for the system containing the interactions of carbon and/or hydrogen. It usually consists of three terms to evaluate the total

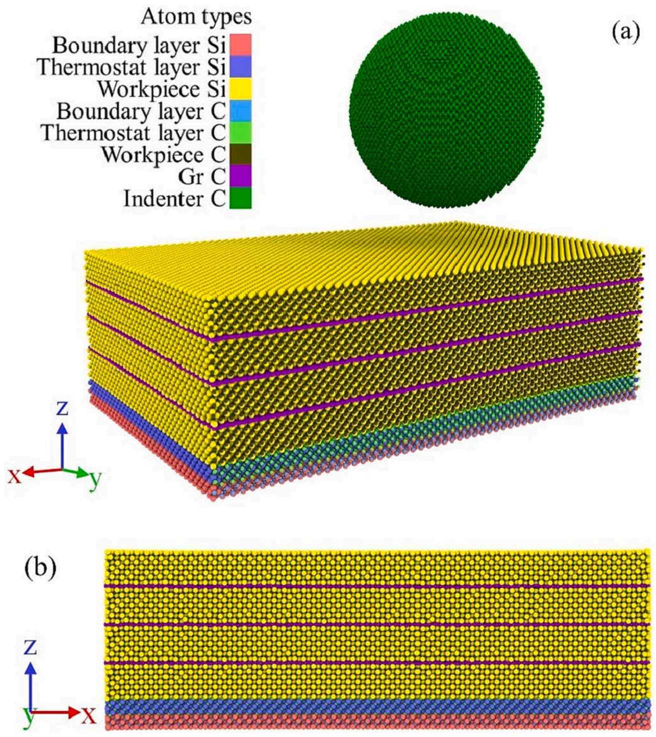

Fig. 1. Simulation model of (a) Gr/3C-SiC nanocomposite with three layers Gr and a diamond indenter and (b) the front view of Gr/3C-SiC nanocomposite laminate.

potential energy *E*. (See Supplementary Eq. (A.1) and (A.2).).

In this work, a software tool called Large-scale Atomic/Molecular Massively Parallel Simulator (LAMMPS) [30] is employed with the visualization code Ovito to complete the simulation [31]. The velocity-Verlet algorithm is implemented to integrate Newton's equation of motion [32]. Also, the time step in scratching simulation is set to 1 fs. After the energy minimization of the structure, the temperature was controlled by Nose-Hoover thermostat, and the pressure was controlled by Nose-Hoover barostat. The workpiece was first relaxed under NVT (constant number of atoms, volume, and temperature) ensemble at 300 K, then NPT (constant number of atoms, pressure, and temperature) ensemble with 300 K and zero pressure was implemented to the simulation in x- and y-direction. A constant downward velocity of 0.2 Å/ps was applied to the indenter under NVT ensemble until it indented at a certain depth in the workpiece and keeps the position until the model was fully relaxed. After that, the indenter moved horizontally with a constant velocity along x-direction. (Scratching on (0 0 1) SiC surface at [1 0 0] direction.) By changing the scratching depth, scratching speed, temperature and the number of Gr layers, the influence of these factors on tribological properties can be studied. The details of the simulation are listed in Table 1.

For the Morse potential used in this simulation, the parameters involved in the interactions between Si atoms and diamond atoms, and between C atoms from SiC or Gr and diamond atoms are listed in Table S1 [25]. It should be noted that the interactions between the atoms in the indenter are ignored and the relative positions of those atoms are fixed to ensure that the indenter is rigid. In scratching simulation, the frictional force and normal force were calculated directly from the command "fix setforce" provided by LAMMPS that can derive the component forces along scratching direction and perpendicular to the scratching direction on the indenter.

2.2. Mechanical properties of Gr/3C-SiC nanocomposite

The testing of mechanical properties such as elastic modulus and tensile strength is critical to ensure that the composite is strong enough to withstand failure during friction. The bulk model with the dimension of $75a \times 62a \times 16a$ (a: lattice constant of SiC) is applied to examine the elastic modulus of Gr/3C-SiC nanocomposite. One of the examples of the corresponding model is depicted in Fig. 2. The periodic boundary condition (PBC) is implemented in all three dimensions. The potentials involved here are the same as the scratching simulation. The system is first relaxed under NPT ensemble with 300 K after energy minimization. Further, the model is deformed with a constant strain rate of 0.001 ps^{-1} in the x-direction to stretch the model until it fractures.

Since PBC is used in this case, the boundary effect caused by the finite size of the model can be ignored. Five gap distances between adjacent Gr layers: 10 Å, 12 Å, 17 Å, 21 Å, and 34 Å are selected to evaluate the elastic modulus and UTS. Different gap distances at the micro level will result in different total amounts of the stacking Gr layers within the SiC at the macro level. It is also noted that with different number of Gr layers, the length of the model in z-direction in the original box would be different, but it will not affect the final result with PBC. The configurations of the tensile loading simulation are exhibited in Table 2.

Table 1
Configurations of the MD simulation for scratching of the laminate.

Configurations	Details
Dimensions	Workpiece: 240 × 150 × 77; distance between adjacent Gr layers: 12, 17, 21; tool: 50 in radius (Unit: Å)
Total number of atoms	330,000
Boundary conditions	p p s
Time step	1 fs
Temperature	300, 500, 700 K
Scratching speed	10, 20, 30, 40, 50, 60, 70, 80 m/s
Scratching depth	10, 20, 30 Å
Scratching length	80 Å
Potentials	Tersoff, AIREBO, Morse

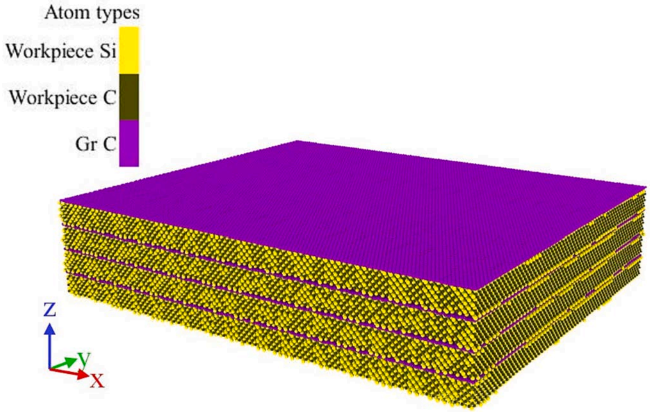

Fig. 2. Gr/3C-SiC nanocomposite model with a gap distance of 17 Å between adjacent Gr layers for tensile test simulation.

2.3. Thermal properties of Gr/3C-SiC nanocomposite

In LAMMPS, the treatment of the thermal conductivity can usually be divided into two methods. The first method is equilibrium molecular dynamics (EMD) evaluation based on the Green-Kubo formulism [33,34], which utilizes the autocorrelation of spontaneous heat flux in the equilibrium state. The second method is non-equilibrium molecular dynamics (NEMD), which is based on the static heat flux in the non-equilibrium state. In this study, NEMD method is implemented in the Gr/3C-SiC nanowire system to calculate the thermal conductivity along the x-direction with different lengths under 300 K. One of the models is shown in Fig. 3.

The simulation model has the same height as the previous studies, which is 65 Å. The width of the model is also the same as its height. The surface of the composite nanowire is set as C-terminated in this simulation of thermal conductivity calculation. After energy minimization, the system is first relaxed under NVT ensemble at 300 K to keep the temperature of the model to be around 300 K. This step can dissipate the potential energy of the system while keeping the initial volume of the system unchanged. Then, NPT ensemble is implemented with zero pressure in all three dimensions while keeping the temperature unchanged. After the volume, temperature, and pressure become stable, the simulation is run with NVE ensemble for 90 ps. Two thermostats are applied to the nanowire model, one with 310 K at the position of $\frac{1}{4}L$, and the other with 290 K at the position of $\frac{3}{4}L$ shown in Fig. 3 (b). A heat flux is then produced between the two thermostats. When the heat flux becomes stable, the average temperatures at different sections of the model along the x-direction are recorded within 300 ps from the simulation. By changing the length of the model in the x-direction, the thermal conductivity in each case can be calculated. The number of Gr layers stacked in SiC is also changed to evaluate its effect on the thermal conductivity.

Table 2
Configurations of the MD simulation for tensile loading of composite.

Configurations	Details
Dimensions	327 × 270 × 69 (Unit: Å)
Distance between adjacent Gr layers	10, 12, 17, 21, 34 (Unit: Å)
Total number of atoms	620,000
Boundary conditions	p p p
Time step	1 fs
Temperature	300 K
Potentials	Tersoff, AIREBO
Strain rate	0.001 ps^{-1}

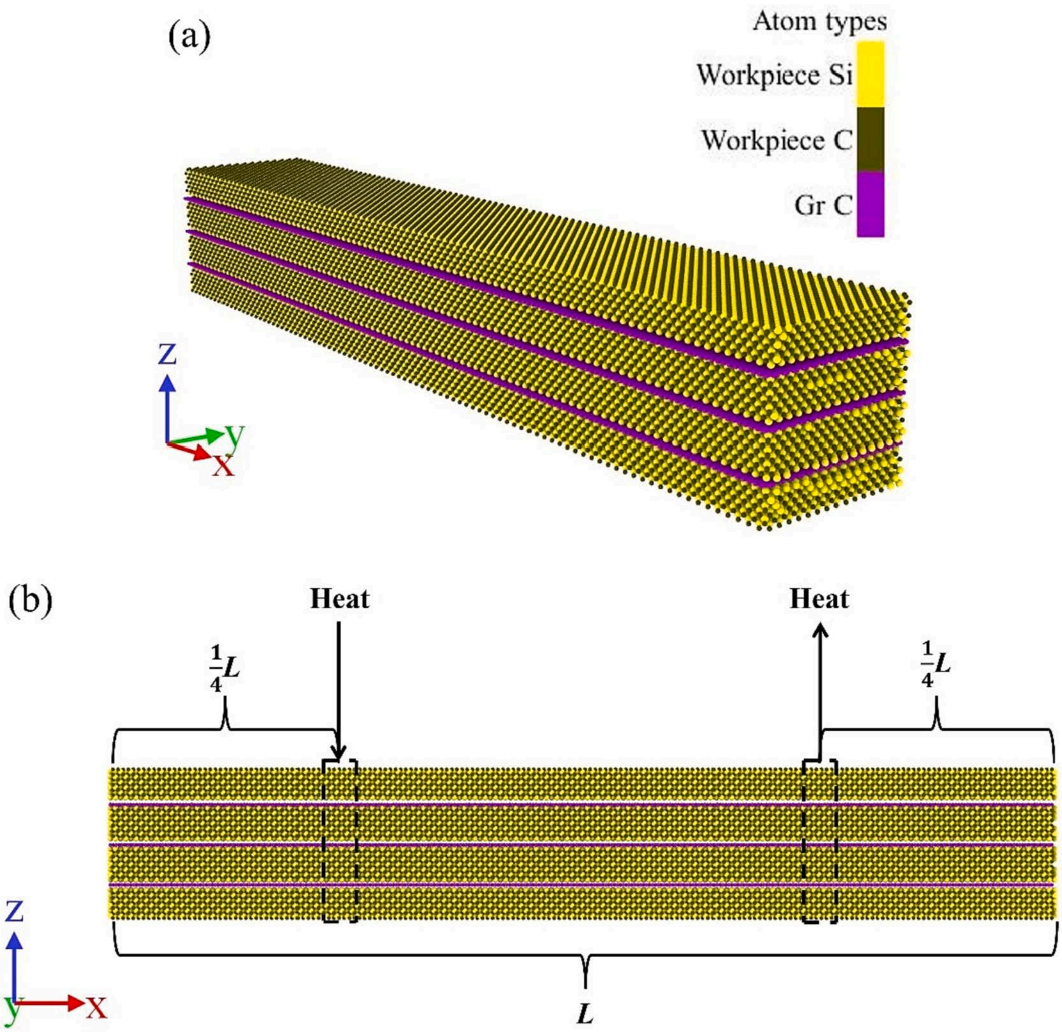

Fig. 3. Simulation model of Gr/3C-SiC nanowire with 3 Gr layers and a length of 400 Å along the x-axis.

Table 3
Configurations of the MD simulation for thermal conductivity of composite.

Configurations	Details
Dimensions	200 (400, 500, 800, 1000) × 65 × 65 (Unit: Å)
Number of Gr layers	2, 3, 4
Boundary conditions	p p p
Time step	0.3 fs
Temperature	300 K
Potentials	Tersoff, AIREBO

Table 3 lists the configurations of the simulation.

The thermal conductivities of pure 3C-SiC with the same sizes and system configurations are calculated. A comparison is then made between the thermal conductivity of Gr/3C-SiC nanocomposite and pure 3C-SiC. Moreover, the number of the stacked Gr layers in SiC is also considered since it could impact the thermal conductivity as it brings different number of interfaces into the laminate [35].

3. Simulation results and discussions

3.1. Tribological properties of Gr/3C-SiC nanocomposite

The frictional force, normal force, and corresponding coefficient of friction with scratching distance from one of the scratching simulations is shown in Fig. 4. The following default configuration were used: scratching depth: 20 Å, scratching speed: 20 m/s, temperature: 300 K, number of Gr layers: 3.

Fig. 4 (a) shows the variations of both frictional force and normal force with scratching distance. At the beginning of the scratching, the normal force is at its largest magnitude, because the indenter has already indented into the workpiece at the end of the indentation process before scratching. There is no frictional force at first since the indenter has not yet moved horizontally. When the indenter starts to move, the normal force drops rapidly from its highest value, because the rear part of the indenter is separated from the workpiece and the total contact area decreases. Compared to the initial status, only half of the indenter gets contact with the workpiece, which will reduce the normal force. On the other hand, the frictional force increases very quickly as the indenter experiences more resistance from the workpiece along the scratching direction. This causes the coefficient of friction to increase as shown in Fig. 4 (b). After a while, both frictional force and normal force tend to remain stable with small fluctuations when the indenter displacement reaches 20 Å due to the thermal motion of the atoms and the movement of the dislocations that may exist in the material [25]. In order to simplify the calculation, the frictional force and normal force are averaged when their values can be considered unchanged. The effective coefficient of friction μ_e is then calculated by using Amontons-Coulomb's law [36] shown in Eq. (1) based on the ratio of the averaged frictional force $\overline{F}$ to the averaged normal force $\overline{N}$.

$$\overline{F} = \mu_e \overline{N} \quad (1)$$

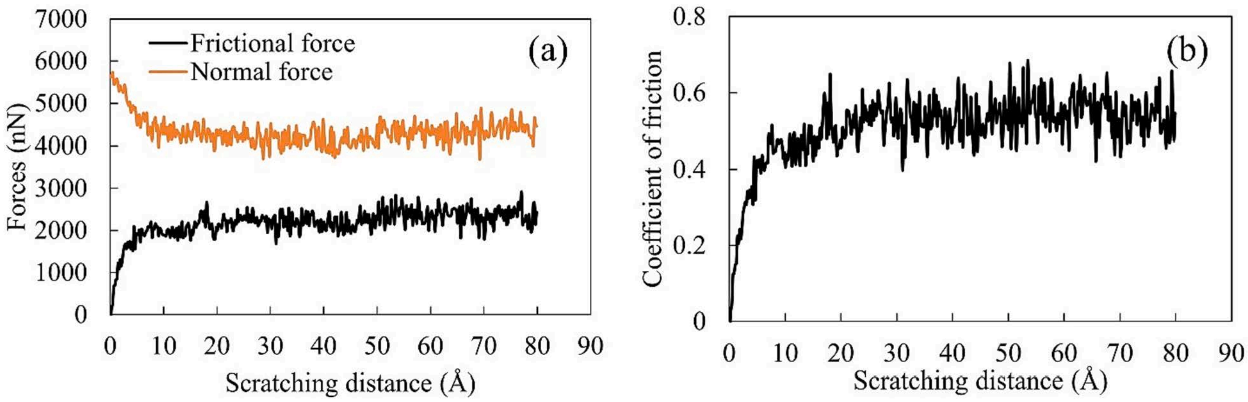

Fig. 4. Profiles of (a) frictional force, normal force, and (b) coefficient of friction versus scratching distance.

The insertion of the Gr layers in 3C-SiC brings interfaces between Gr and 3C-SiC, which can play an important role in the tribological, mechanical, and thermal properties of the nanocomposite laminate. As mentioned before, the interaction between Gr layer and SiC can be either strong or weak. And usually, it is easier to form weak interactions, which is led by VdWs force. Therefore, it is worth comparing covalent bonding interactions and weak interactions and examining the stability of the interface. We used pure bulk 3C-SiC, pure single layer Gr, and mixed nanocomposite, all with the same sizes as the model implemented in the simulation of scratching. The sample 3C-SiC is just the same as one of the pieces of 3C-SiC between two adjacent Gr layers shown in Fig. 1, which has a dimension of 240 × 150 × 13 (unit: Å). The single layer Gr has a dimension of 240 × 150 (unit: Å). The mixed nanocomposite is the combination of two 3C-SiC pieces with one Gr layer stacked in the middle. For the case with weak interactions, Lennard-Jones (LJ) potential was employed. (See Supplementary Table S2 for parameters of LJ potential [37].) With these values being derived, the interfacial energy per unit area, $E_{\text{interface}}$, can be calculated using the following equation [38].

$$E_{\text{interface}} = \frac{E_{\text{mix}} - (2E_{\text{SiC}} + E_{\text{Gr}})}{2A} \tag{2}$$

In the equation, E_{sic} is the potential energy of the single piece of 3C-SiC prior to mixing, E_{Gr} is the potential energy of the single layer Gr prior to mixing, E_{mix} is the potential energy of the mixed nanocomposite, and A represents the area of the interface between 3C-SiC and Gr. The potential energy for each model and the final calculated interfacial energy per unit area are listed in Table 4 and Table 5, respectively.

From Table 4 and Table 5, the interfacial energy per unit area for both with covalent bonding and VdWs interactions are negative, which indicates they can form stable interfaces between Gr and SiC. But the magnitude with covalent bonding or strong interactions is much larger than that with VdWs interactions. That means the stability of the interface in the former case is better than the latter case. And it may result in better material properties when the interfacial energy is lower [38].

3.1.1. Effect of scratching depth

The scratching depths of the indenter with 10 Å, 20 Å, and 30 Å with other configurations fixed (scratching speed of 20 m/s, temperature of 300 K, and 3 Gr layers) are taken into account to study its effect on the tribological properties. The surface topography and the profile in the front view of the workpiece with three different scratching depths can be seen in Fig. 5.

Table 4
Potential energy for different models.

Energy	Value (10^{-13} J)
E_{SiC}	−0.452
E_{Gr}	−0.159
E_{mix} with covalent interactions	−1.16
E_{mix} with VdWs interactions	−1.07

Table 5
Interfacial energy with different interaction types.

Interaction type	Interfacial energy per unit area (J/m^2)
Covalent interactions	−13.16
VdWs interactions	−0.41

Apparently, in Fig. 5, with a larger scratching depth, more deformation takes place in the contact area and more worn atoms are produced on the top of the workpiece. This is mainly because the contact area between the indenter and the workpiece in both transverse and normal directions increases with the scratching depth, which would lead to higher frictional forces and normal forces shown in the following discussion. This results in more deformation on workpiece and generates more wear in the front of the indenter. Table 6 shows the averaged frictional force, averaged normal force, and effective coefficient of friction of both Gr/3C-SiC nanocomposite and perfect single crystal 3C-SiC with the same size.

From Table 6, it can be found that for the Gr/3C-SiC nanocomposite and the 3C-SiC models, both frictional force and normal force become

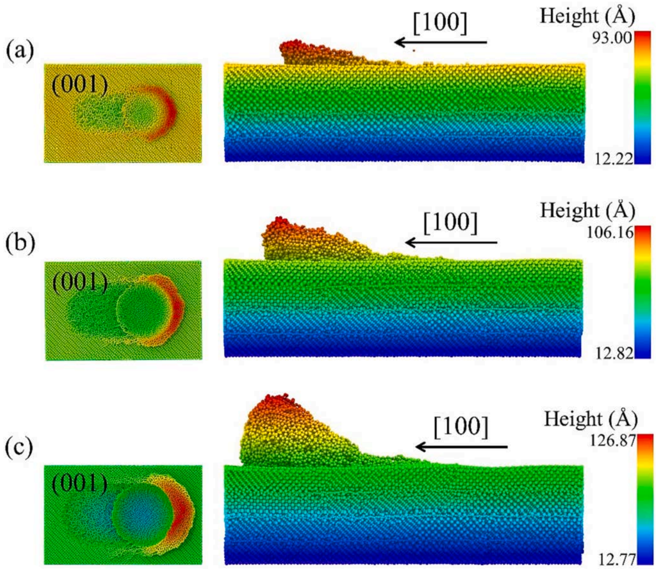

Fig. 5. Surface topography and profile in the front view of the workpiece with scratching depth of (a) 10 Å (b) 20 Å, and (c) 30 Å.

Table 6
Averaged forces and coefficient of friction of Gr/3C-SiC nanocomposite and 3C-SiC.

Model	Scratching depth (Å)	Averaged frictional force (nN)	Averaged normal force (nN)	Effective coefficient of friction
Gr/3C-SiC nanocomposite	10	1085.43	1957.03	0.55
	20	2321.20	4286.66	0.54
	30	4156.16	5699.26	0.73
3C-SiC	10	1465.26	2747.47	0.53
	20	2787.90	4680.54	0.60
	30	4225.21	6164.68	0.69

larger with deeper scratching depth. For pure SiC, the coefficient of friction increases with the increase of scratching depth, because the frictional force grows faster than the normal force. Although for Gr/3C-SiC nanocomposite the coefficient of friction was smaller when the scratching depth was 20 Å compared to the case when it was 10 Å, it still showed an increasing trend with a larger scratching depth. This is due to the frictional force increasing slowly than the normal force when the scratching depth increases from 10 Å to 20 Å. Meanwhile, when the scratching depth increased to 30 Å, the growth speeds for the two forces are reversed. The coefficient of friction of the laminate is similar compared to that of the SiC with the scratching depth of 10 Å and 20 Å, but it becomes higher than that of SiC with the scratching depth of 30 Å. Compared to SiC under the same scratching depth, Gr/3C-SiC nanocomposite experiences smaller frictional force and normal force. The lubrication characteristics exhibited by Gr layers could explain the reason why the indenter experienced resistance which was accompanied by shear on the workpiece [39]. On the other hand, the fact that Gr layer can be easily deformed in the out-of-plane direction could help the indenter press into the workpiece with a smaller normal force. The trends represented in Table 6 are very similar to the result in the literature [25] regardless of the different configurations of the workpiece used, which testifies that the result here is valid.

By analyzing the amount of the worn atoms produced during the whole friction process, the wear rate of both the laminate and the SiC can be evaluated. It can also be verified that the volume of the worn atoms has a linear relationship with the scratching distance as described by the Archard wear equation [40].

$$V = \frac{KFL}{H} \tag{3}$$

Where V is the total volume of worn atoms produced; K is a dimensionless constant, which can be also called wear coefficient. F is the total normal force; L is the sliding distance and H is the hardness of the softest contacting surfaces. In this simulation, the volume of the atoms of the worn atoms was computed through Voronoi Tessellation method provided by LAMMPS [41,42]. the wear rate can be handled by using the ratio of V and L, which is the volume loss per unit sliding distance. As the hard indenter scratches the workpiece, wear debris is produced and piled up in front of the indenter as shown in Fig. 5. However, the volume of the wear debris or worn atoms varies with the threshold height defined above the top surface of the laminate. A higher threshold would certainly result in a smaller volume of worn atoms, but it will not affect the results from the wear. Here, half of the lattice constant of 3C-SiC is selected (about 2.18 Å) as the threshold height. The curves of the volume of worn atoms produced with the scratching distance at various scratching depths are shown in Fig. 6.

From Fig. 6, it follows that before scratching distance reached 8 Å, there was almost no worn atoms generated for all the three varied depths. Further, as the indenter keeps scratching on the surface of the workpiece, the volume of worn atoms increases linearly, which validates the Archard wear equation. The wear rate of the material was calculated using the total volume of the worn atoms divided by the total scratching distance. The comparison between the Gr/3C-SiC nanocomposite and the pure 3C-SiC on wear rate is exhibited in Table 7.

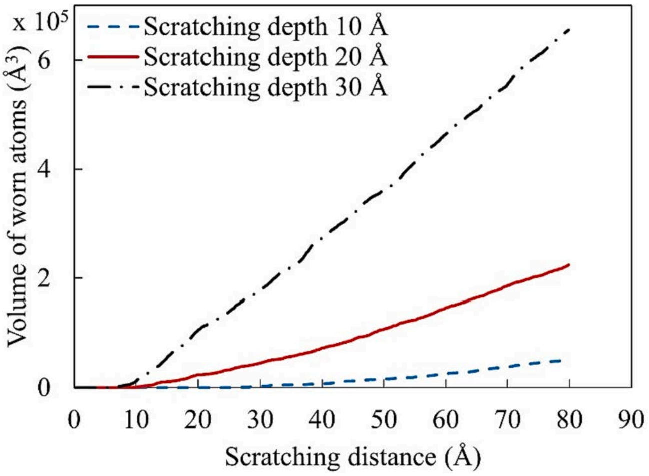

Fig. 6. Volume of worn atoms versus scratching distance with various scratching depth.

Table 7
Wear rate of Gr/3C-SiC nanocomposite and pure 3C-SiC with various scratching depth.

Model	Scratching depth (Å)	Wear rate (nm^3/nm)
Gr/3C-SiC nanocomposite	10	6.53
	20	28.06
	30	82.06
3C-SiC	10	15.43
	20	54.69
	30	121

Clearly, in both models, a larger scratching depth would cause a higher wear rate. Also, considering the scratching depth, the SiC with stacking Gr layers generates fewer worn atoms. The reduction rate of the wear rate is about 57.68 %, 48.69 %, and 32.18 % for the scratching depth of 10 Å, 20 Å, and 30 Å between two materials, respectively. Again, this is mainly due to the lubrication of the Gr layers inside the workpiece [39], which can significantly improve the wear resistance of the material.

During the scratching process, both elastic and plastic deformations take place on the surface and inside the laminate. The two types of deformations mix and lead to internal stress. To understand the effect of friction on the internal stress and how the internal stress develops, the von-Mises stress distribution of the workpiece is implemented. Von-Mises stress is to determine if the material will yield or fracture. (See Supplementary Eq. (A.4) [25]) The von-Mises stress of each atom in the workpiece is calculated and combined to obtain the spatial von-Mises stress distribution of the workpiece. Fig. 7 shows the spatial stress distribution of the workpiece in the cross-sectional view at the position where the scratching distance is 0, 40 Å and 80 Å, respectively. The rest of the configurations are the same as before.

When the indenter completes the indentation process for the same condition as in Fig. 7 (a), the regions around the indenter show high stresses. The portion of the Gr layers below the indenter also gets

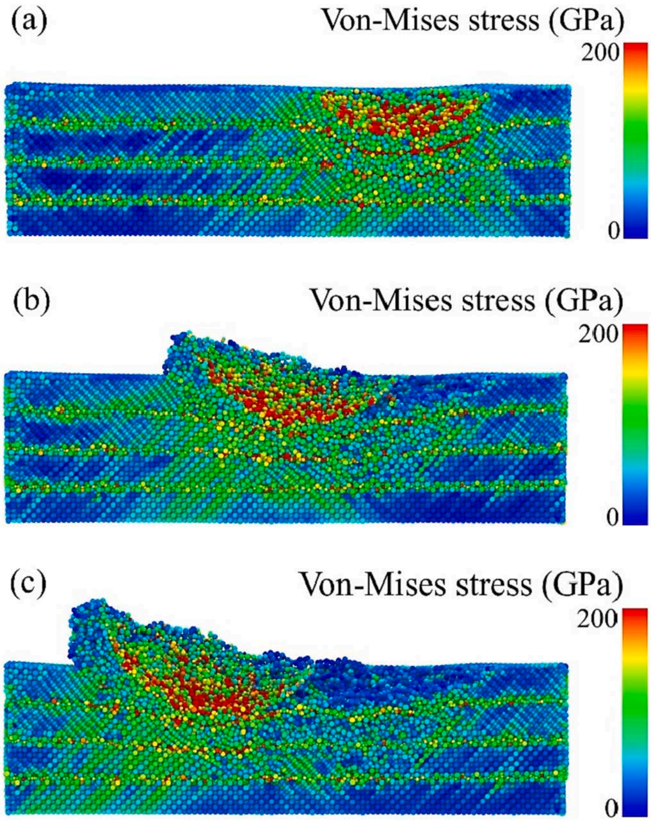

Fig. 7. Spatial von-Mises stress distribution in the cross-sectional view of the workpiece at the scratching distance of (a) 0, (b) 40 Å, and (c) 80 Å.

deformed and results in relatively high stress along the Gr layers. As the indenter moves to the middle and towards the end of the workpiece, a high stress level is always detected near and below the indenter and in the Gr layers during the whole scratching process. In addition, the stress in the regions of the SiC phase where the indenter passes through also reduces. The spatial stress distributions of the laminate and pure SiC with different scratching depths at the end of the scratching process are presented in Fig. 8.

In Fig. 8, it is obvious that large elastic and plastic deformation takes place around the indenter. Also, high stress is observed in the areas near the indenter and Gr layers. The larger the scratching depth, the more internal stress is generated. The large scratching depth can destroy the original structure of the laminate as well by disturbing the Gr layers, which is shown in the area of the workpiece in front of the indenter in Fig. 8 (c). Therefore, the stress in the SiC phase near the Gr layers becomes higher than that under smaller scratching depth. In the pure SiC model, high stress also occurs around and below the indenter. The region under the indenter where the indenter just finishes the indentation process still has very high stress at the end of the simulation, while in the laminate, the stress in the same position is partially transferred to the Gr layers. That means the Gr layers can help SiC phase bear the high internal stress in the laminate, which may reduce the early failure of SiC in friction.

The spatial temperature distributions of both the composite laminate and the pure SiC with different scratching depths are considered in the next step. The results can be visualized in Fig. 9.

Similar to spatial stress distribution, in the laminate, the region near the indenter during scratching has the highest temperature. The temperature is lower in the region far from the indenter. In addition, the thermal softening becomes more obvious due to higher temperature with larger scratching depth, which is one of the reasons why more worn atoms were generated [25]. The pure SiC model follows the same pattern here, and it seems that the spatial temperature distributions of the two cases are almost the same, despite that more worn atoms were produced in SiC than in the laminate. Based on the results of wear rate, spatial stress distributions and spatial temperature distributions, apparently it is suitable for the friction with a small scratching depth to have low wear rate, low internal stress and weak thermal softening effect. In this work, the scratching depth of 10 Å would be the best for

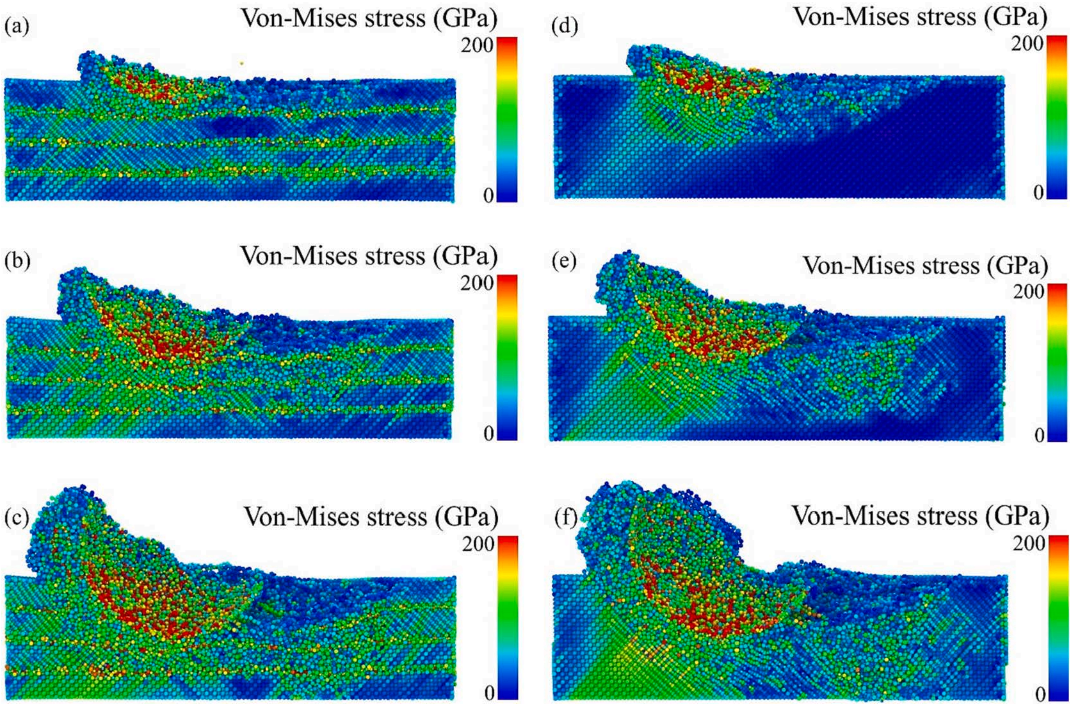

Fig. 8. Spatial von-Mises stress distribution in the cross-sectional view of the Gr/3C-SiC nanocomposite with the scratching depth of (a) 10 Å, (b) 20 Å, and (c) 30 Å, and 3C-SiC with the scratching depth of (d) 10 Å, (e) 20 Å, and (f) 30 Å.

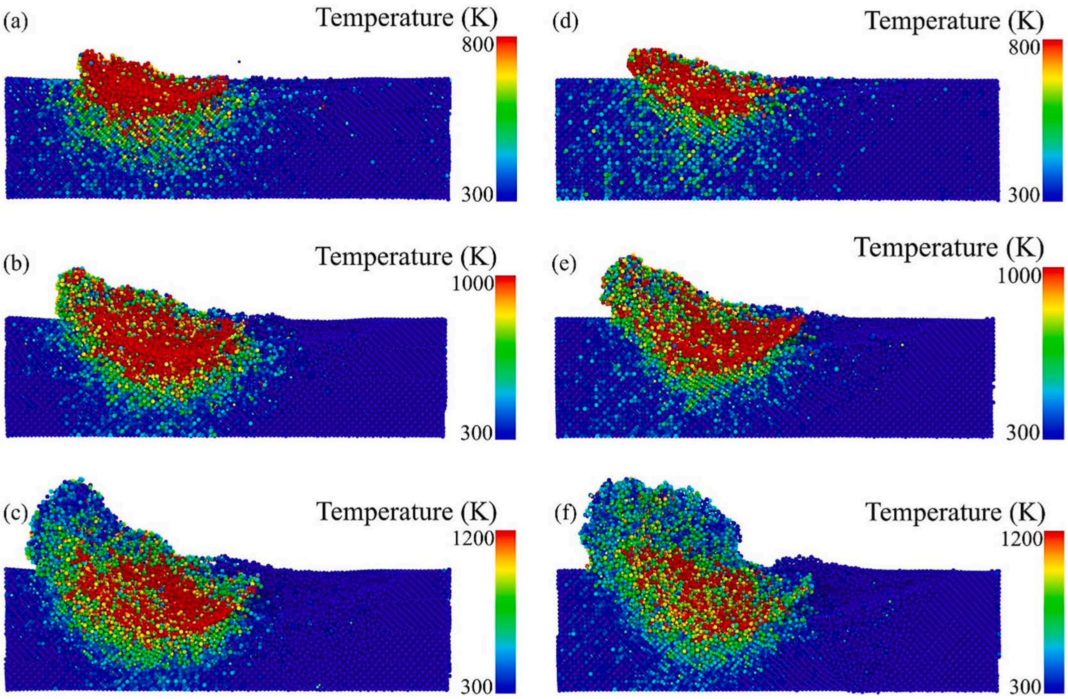

Fig. 9. Spatial temperature distribution in the cross-sectional view of the Gr/3C-SiC nanocomposite with the scratching depth of (a) 10 Å, (b) 20 Å, and (c) 30 Å, and 3C-SiC with the scratching depth of (d) 10 Å, (e) 20 Å, and (f) 30 Å.

keeping the performance of the friction material, since it shows similar coefficient of friction as when scratching depth is 20 Å and much lower wear rate compared with the case when scratching depth is 30 Å even though the latter one has a higher coefficient of friction. It is noteworthy that in automotive industry, usually there is a certain range of the achievable values for the coefficient of friction. Given a high coefficient of friction, less pressure would be needed to create a sufficient braking force. On the other hand, if the coefficient of friction is too high, it could create more wear and reduce the service life of the brake pads. A stable capacity of braking is very important. Thus, there is a trade-off between a high coefficient of friction and a low wear rate, and it is difficult to designate the best result here.

3.1.2. Effect of scratching speed

The influence from the scratching speed of the indenter on the surface of the workpiece is also taken into consideration in this study. A range between 10 m/s and 80 m/s with the interval of 10 m/s as the scratching speed of the indenter is used, which is very close to the normal driving speed of a passenger vehicle. The final result shows that, as the scratching speed increases form 10 m/s to 80 m/s, the averaged frictional force fluctuates between approximately 2253 nN and 2389 nN, while the averaged normal force fluctuates between approximately 4287 nN and 4464 nN, resulting in the effective coefficient of friction with the range from 0.52 to 0.54. The forces and corresponding coefficient of friction with various scratching speeds are depicted in Fig. 10.

Different from the other literature with respect to the study for the effect of the scratching speed in a very huge range [25], in such a relatively small velocity range for the indenter, the frictional force and the normal force are not influenced very much. This also brings a stable effective coefficient of friction with very limited change. Although the prior researchers have found that with different types and compositions of the friction composite, the coefficient of friction can vary with the sliding speed, they also pointed out that the coefficient of friction is not as sensitive to the sliding speed as the pressure and other loading [43]. Since this work only considers dry friction without changing the content of the material when scratching speed varies, it is reasonable that coefficient of friction does not represent significant change with different scratching speed since the forces only show small fluctuations. But again, this conclusion is valid only within the speed range in Fig. 10. In Fig. 11, it can be noticed that the wear rate in each scenario is also very close to each other.

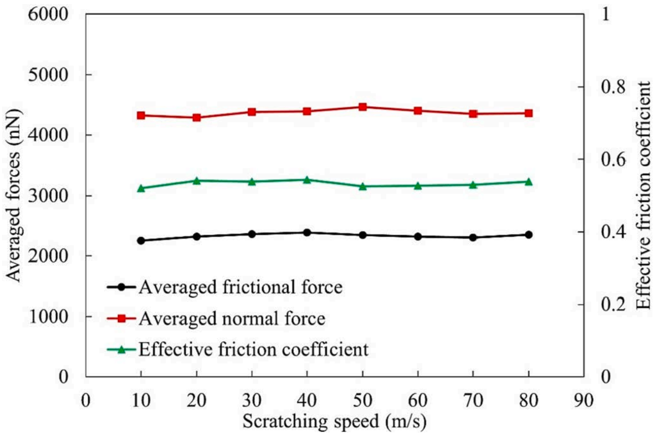

Fig. 10. Averaged forces and effective coefficient of friction with scratching speed.

This indicates that the severity of wear is very similar in each case. However, since the scratching speed is also not the same, thus, a higher scratching speed tends to produce more wear debris within the same scratching time. By analyzing three typical spatial temperature distributions of the workpiece with different scratching speeds, the effect of the scratching speed on the wear is more obvious to observe.

During the scratching, the strain rate hardening and thermal softening usually play an important role in the forces encountered by the indenter from the workpiece, and the deformation and the wear of the workpiece [25]. But in this work, the main material is SiC, which is a brittle ceramic with a relatively low ductility, and the amount of dislocations generated in the material is very limited. This is also visualized in the simulation results. Moreover, the effect of strain rate hardening is

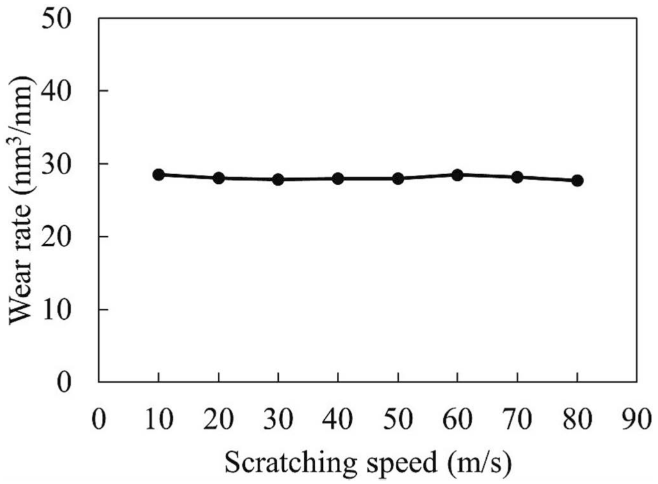

Fig. 11. Wear rate at various scratching speeds with the same scratching distance.

largely reduced, and thermal softening is dominated during the simulation. To exhibit the influence of scratching speed on the temperature, three scratching speeds: 10 m/s, 40 m/s, and 80 m/s, respectively, are selected in Fig. 12. It is obvious that the temperature of the workpiece around the indenter is the highest, and at a higher scratching speed, the temperature becomes higher and leads to more appreciable thermal softening effect, which increases the wear rate and reduces fade resistance. In conclusion, the smaller the scratching speed, the better for the friction material to maintain its tribological performance. It has been found that a scratching speed of 10 m/s leads to the best performance for the friction material.

3.1.3. Effect of temperature

As discussed previously, the temperature of the model can largely affect its tribological properties. Therefore, three different system temperatures: 300 K, 500 K, and 700 K are implemented using the same simulation configurations with a scratching depth of 20 Å. The results are listed in Table 8.

Based on the data in Table 8, it can be seen that at a higher temperature, the thermal softening becomes more severe, resulting in smaller frictional forces and normal forces. The coefficient of friction also decreases from 0.54 to 0.51 at this temperature range due to a faster decrease in the frictional force than the normal force. This trend is in agreement with the previous work using a similar process but with a different model [25]. The main reason to cause such a trend is that the elevated temperature led to an increase in the kinetic energy of the atoms and caused the thermal softening effect in workpiece. This made the deformation easier to take place during friction, and thus, produced smaller frictional and normal forces. In addition, a higher temperature can reduce the free energy of the system, which can be responsible for the decrease of the interatomic force [44], resulting in a smaller adhesive force on the interface between the indenter and the workpiece. This is possibly-one of the reasons why the coefficient of friction becomes smaller at higher temperatures. The thermal softening effect reduces the resistance the atoms experience during the movement because the material becomes softer and the atoms are easier to move with higher internal energy. Therefore, the scratching process can produce more worn atoms at higher temperatures. This also brings another possible reason to cause smaller coefficient of friction that the transfer film of the worn atoms from the workpiece between the sliding surfaces could be well developed at elevated temperatures and reduces the frictional force [15,45]. In Table 8, the calculated wear rate increases when the system temperature goes up from 300 K to 700 K, which agrees with the analysis above. We believe that the friction material reaches an optimal performance in terms of both a relatively high coefficient of friction and a low wear rate at a temperature around 300 K.

Table 8
Averaged forces, coefficient of friction, and wear rate of the laminate at various temperatures.

Temperature (K)	Averaged frictional force (nN)	Averaged normal force (nN)	Effective coefficient of friction	Wear rate (nm^3/nm)
300	2321.20	4286.66	0.54	28.06
500	1830.75	3475.11	0.53	29.76
700	1640.07	3233.12	0.51	32.19

3.1.4. Effect of the number of Gr layers

Despite that the bond type is fixed and defined as covalent bonding between SiC and Gr layers, the number of stacked Gr layers within the SiC may also be a factor to affect the structure of the material and vary the tribological properties. Without changing the size of the model, the numbers of Gr layers alternate with the SiC at an even spacing. Table 9 shows the tribological data obtained from the scratching simulations with different numbers of Gr layers.

Due to the lubrication and the relatively flexible shape in the out-of-plane of the Gr layers with low adhesion and surface energy, both frictional forces and normal forces would tend to decrease with more Gr layers [39]. This is in agreement with the results in Table 9. As the number of Gr layers increases from two to four, the frictional forces and

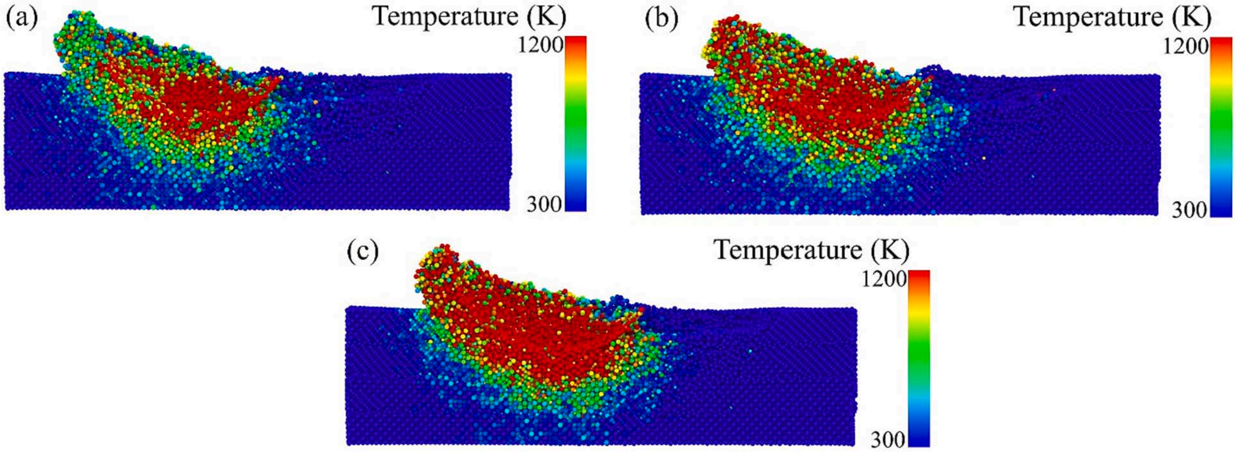

Fig. 12. Spatial temperature distributions of the workpiece with the scratching speed of (a) 10 m/s, (b) 40 m/s, and (c) 80 m/s.

Table 9
Averaged forces, coefficient of friction, and wear rate of the laminate with various number of Gr layers.

Number of Gr layers	Averaged frictional force (nN)	Averaged normal force (nN)	Effective coefficient of friction	Wear rate (nm^3/nm)
2	2555.84	4326.84	0.59	46.01
3	2321.20	4286.66	0.54	28.06
4	2038.09	4007.41	0.51	21.44

normal forces show a decreasing trend. The coefficient of friction also drops from 0.59 to 0.51. In addition, a better wear resistance the material was observed when more Gr layers were stacked. From two Gr layers to four Gr layers, the wear rate was reduced about 53.4 %. It implies that Gr layer has a great potential in improving the wear behavior in friction materials. From Fig. 13, it seems that the effect of the Gr layer number on the stress and temperature is not so obvious. There is actually an appreciable stress concentration in the interior of the workpiece in all three cases. The volume of worn atoms also decreases due to improved lubrication by Gr. We conclude that the number of stacked Gr layers in 3C-SiC can affect the friction and wear performance. A few numbers of stacked Gr layers would result in a higher coefficient of friction, but at the same time would lead to more severe wear. From Table 9, the case with three Gr layers is possibly better due to its relatively high coefficient of friction and a much smaller wear rate compared to the case with two Gr layers.

We can also analyze the effect of the number of Gr layers by plotting the mass density profile of Gr atoms as a function of the workpiece height shown in Fig. 14.

Fig. 14 (a) – (c) are the local mass density profiles of Gr atoms along the z-direction (workpiece height) in the model with two Gr layers, three Gr layers, and four Gr layers, respectively. To calculate local mass density profile, the material was binned with a thickness of 0.05 Å along the z-direction. The mass density was then determined by the ratio between the total mass of Gr atoms in a bin and the volume of the bin. The black curves are the mass density profiles before the indentation, and the orange curves are the mass density profiles after the scratching process. In each case, the peak of the black curve shows a decreasing trend of height and an increasing trend of width with larger workpiece height. By analyzing the simulation results, we conclude that the higher the Gr layer is located in the workpiece, the lower flatness of the surface it has, and this is especially apparent for the case with four Gr layers as the rightmost black peak only reaches around 4 g/cm^3 while with a wider range. The reason to cause such result is probably that the surface topography of the bulk 3C-SiC is far from the boundary layer, It is harder for the material to keep flat and lead to more roughness of the bonded Gr layer. During the scratching, the normal force from the indenter deformed the Gr layers and resulted in lower and wider mass density peaks. With less stacked Gr layers, the flatness of the interfaces in the workpiece changed more after scratching compared with that before indentation. The workpiece with more Gr layers shows better flexibility and therefore received less external force from the indenter. This helps produces smaller normal and frictional forces, which also agrees with the result in Table 9.

3.2. Mechanical properties of Gr/3C-SiC nanocomposite

The whole simulations of the tensile loading of the nanocomposite with different gap distance between adjacent Gr layers are very similar. The visualization of the tensile simulation with a gap distance of 17 Å between adjacent Gr layers as an example is exhibited in Fig. 15.

At the beginning, the model was in its initial size without any external load. After the uniaxial tensile loading was exerted to the model along × direction, the model was pulled and elongated. When the model was stretched to a certain extent, it became fracture somewhere in the middle. Fig. 16 presents the stress–strain curves from the uniaxial tensile loading simulations of the Gr/3C-SiC nanocomposite with different gap distances between adjacent Gr layers, and the pure bulk 3C-SiC with the same size.

From the stress–strain curves, the composite model only shows a linear relationship between stress and strain when the strain is sufficiently small. The mechanical behavior of the pure bulk SiC is similar to that of the Gr/3C-SiC nanocomposite. When the model breaks, the stress suddenly drops from the highest point to 0. To evaluate the elastic modulus, here we only pick up the frontmost region of the curve and calculate the slope using linear fitting. The parameters used in Fig. 16 are listed in Table 10.

Fig. 16 and Table 10 revealed that the pure bulk SiC has both the smallest Young's modulus and UTS in the six models, but it has a high failure strain compare to other cases. In Gr/3C-SiC nanocomposite, with the gap distance becoming smaller from 34 to 10 Å, Young's modulus also increases from 515.88 to 579.25 GPa. The tensile strength increases from 70.47 to 98.20 GPa. In general, the failure strain gets higher as well when the gap distance between Gr layers becomes smaller except that it gets lower with the gap distance of 12 Å. In fact, the covalent bonds between SiC and Gr would lead to strong interface interactions, which can restrain the deformation of the SiC and Gr [9]. However, damages would be formed and grown from the interfaces as a result of the insertion of the Gr into SiC during tensile loading. When the extent of the damage reaches a certain level, the laminate would get fractured. This probably explains why pure SiC has a high failure strain without any interface inside. In conclusion, the insertion of the Gr layers into the SiC

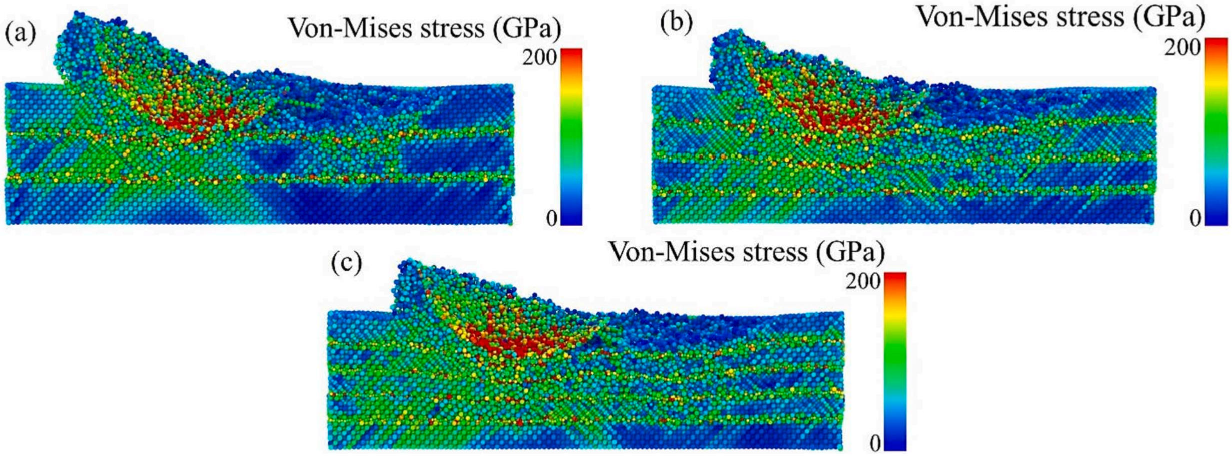

Fig. 13. Spatial von-Mises stress distribution in the cross-sectional view of the Gr/3C-SiC nanocomposite with the number of Gr layers of (a) 2, (b) 3, and (c) 4.

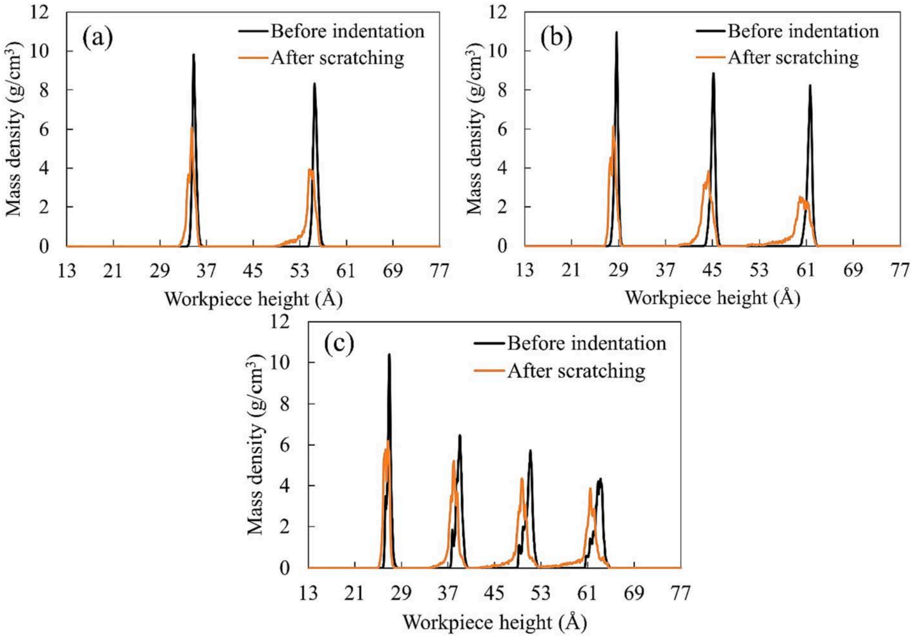

Fig. 14. Mass density profiles of Gr atoms along the workpiece height with (a) 2 Gr layers, (b) 3 Gr layers, and (c) 4 Gr layers.

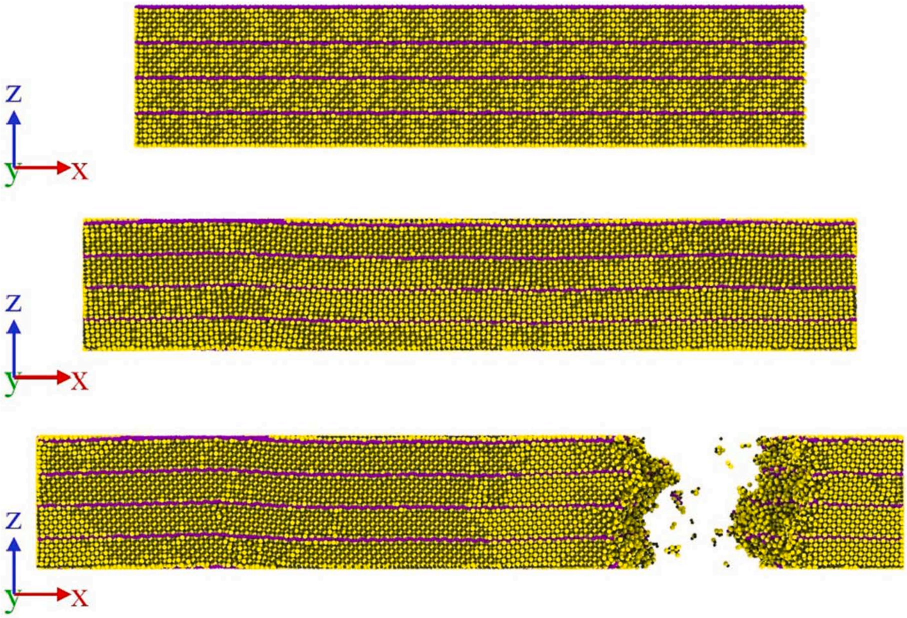

Fig. 15. Visualization of the tensile loading to Gr/3C-SiC nanocomposite (17 Å between adjacent Gr layers).

can significantly improve both Young's modulus and tensile strength of the material, since high Young's modulus and tensile strength of the Gr can promote higher stiffness and stronger atomic forces in composites. The stable covalent bonding between Gr and SiC and the excellent mechanical properties of Gr layers would provide higher load transfer efficiency and interlaminar adhesion, which can enhance the strength of the composite [46]. With better interfacial interactions, Young's modulus and UTS can increase with the Gr layer number. In addition, the limit number of Gr layers between SiC will provide more resistance to the tensile deformation in SiC, which increases the strain to cause material failure. Although there are not so many experimental data for tensile strength of covalent bonded Gr/3C-SiC nanocomposite, it is still easy to find out that the tensile strength of the pure SiC is much higher than that obtained from the real experiment. One reason is that in MD simulation, the material is usually constructed as perfect crystal without any defect. Another important reason is related to the configurations of the simulation. It has been already confirmed that the strain rate can significantly vary the tensile strength [47,48]. The 0.001 ps^{-1} strain rate used in this study seems very large compared with the strain rate used in the experiment, which can cause higher tensile strength. What's more, even though the simulation is done with PBC, the influence of the boundary effect cannot be eliminated completely. By expanding the volume or the size of the model, the tensile strength will get higher to a certain extent as well. The trend of the result here shows that a smaller gap distance between adjacent Gr layers or a higher number of Gr layers stacked in the workpiece leads to a better Young's modulus, tensile strength, and failure strain. As a result, the model with 5 stacked Gr layers would be the best configuration. Although there is not much study

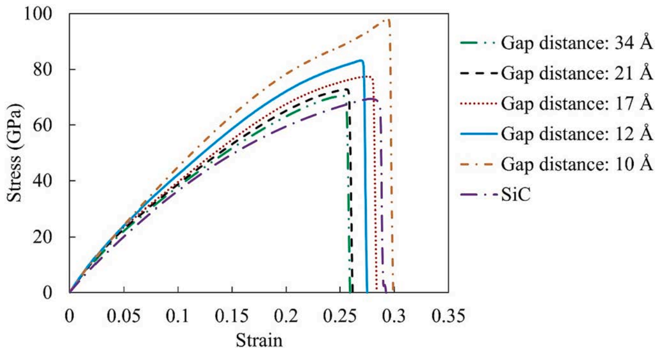

Fig. 16. Stress–strain curves of the Gr/3C-SiC nanocomposite model with different gap distance between adjacent Gr layers and the pure 3C-SiC.

Table 10
The mechanical parameters of the Gr/3C-SiC nanocomposite and bulk 3C-SiC.

Materials		Elastic modulus (GPa)	Tensile strength (GPa)	Failure strain
Gap distance in Gr/3C-SiC nanocomposite	34 Å	515.88	70.47	0.252
	21 Å	542.92	72.81	0.255
	17 Å	569.76	77.46	0.275
	12 Å	577.28	83.19	0.268
	10 Å	579.25	98.20	0.294
3C-SiC		448.93	69.38	0.278

on the mechanical properties of exactly the same type of Gr/3C-SiC nanocomposite used in this work, we can still find some literature using similar models and make comparisons. For example, Zhan et al. [9] constructed bulk 3C-SiC with Gr stacking in between serving as buffer layers and continuous layers, respectively, and showed close values of Young's modulus and tensile strength. They claimed that with more Gr layers inside, both Young's modulus and tensile strength become larger, which is consistent with the conclusion above. The same trend was obtained by Barfmal et al [10] as well.

3.3. *Thermal conductivity of Gr/3C-SiC nanocomposite*

In the study of thermal conductivity of Gr/3C-SiC nanocomposite, the main purpose is to make comparison between the composite and the pure SiC. Therefore, it is not necessary to use large model to get the thermal conductivity which is very close to the bulk material in macro scale. To calculate thermal conductivity, Fourier's law [49] is used here.

$$J = -\kappa \nabla T \tag{4}$$

In Eq. (4), J is the steady heat flux along the nanowire, κ is the thermal conductivity, and ∇T is the temperature gradient between the locations with highest and lowest temperature values. The profile of the temperatures at different positions of the nanowire for each case will just look like Fig. 17.

With the local temperature at each position of the nanowire, the temperature gradient can be calculated easily. The total simulation time, the total energy changed during the simulation and the cross-sectional area of the nanowire are also able to be obtained and will be used for the calculation of the heat flux in Eq. (5).

$$J = \frac{0.5(E_{\mathrm{import}} + E_{\mathrm{export}})}{2At} \tag{5}$$

where E_{import} and E_{export} are total input energy to the system and total output energy from the system, respectively. t is the simulation time, and A is the cross-sectional area of the nanowire. Because PBC is applied in x-direction, the heat imported from the heat source will flow to both sides. Similarly, the heat sink receives heat from both sides. Hence, the whole result needs to be divided by 2 as shown in Eq. (5). By using both Eq. (4) and Eq. (5), the thermal conductivities of the SiC nanowire and the laminate with different numbers of Gr layers for different model lengths can be calculated (See Supplementary Table S3-S5). The results are shown in Fig. 18.

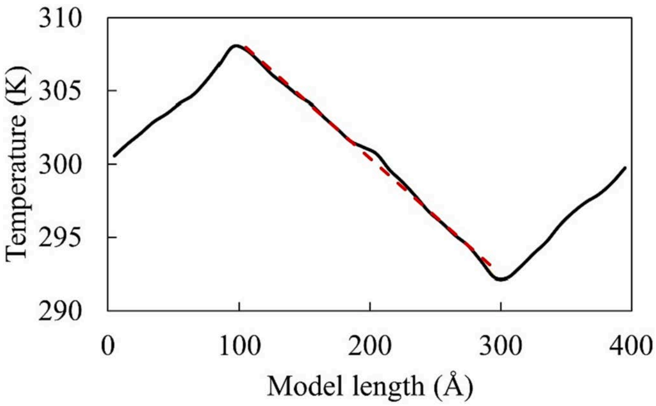

Fig. 17. Variation of the local temperature along the nanowire with the total model length of 400 Å and 3 stacking Gr layers.

Fig. 18 indicates that the thermal conductivity of the nanowire is between 4 and 7 W/mK. With larger model length, the thermal conductivity shows an increasing trend. This is because the larger the model, the closer the size to the real bulk material. Theoretically, if the model was to be lengthened to be extremely long, the result would be very close to the actual thermal conductivity of its bulk material in macro scale without considering the quantum effect on phonon scattering and the defect inside the model [50]. Since the main objective in this section is to analyze the impact of the Gr layers on the thermal conductivity of the material, it is insignificant to calculate the real thermal conductivity of the bulk material. It can also be noticed in Fig. 17 that the pure SiC nanowire represents the highest thermal conductivity, while the laminate shows lower thermal conductivity with more Gr layers. In fact, although Gr layer itself has a very good thermal conductivity, when it is combined with other materials such as SiC by covalent bonds, those covalent bonds will provide the channels in the interfaces between SiC and Gr layers for the phonons to scatter in radial direction but not along the axial direction of the nanowire [18]. The insertion of more Gr layers would just bring more interfaces and make the phonon scattering more severe. The initial high in-plane thermal

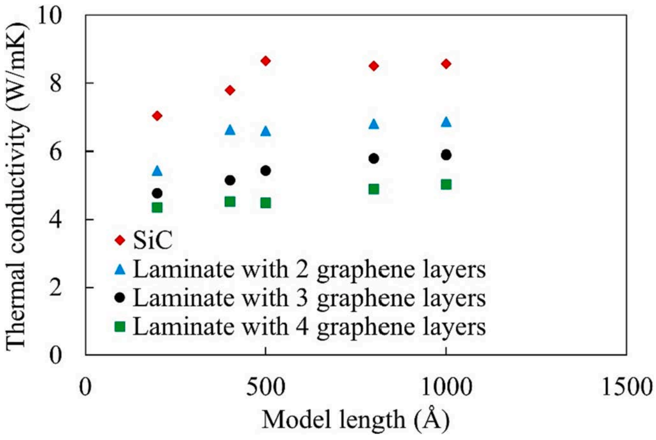

Fig. 18. Thermal conductivities of the nanowires with various model lengths.

conductivity of Gr is due to the sp^2 hybrid bonds on carbon atoms. [8] When Gr is in contact with a substrate covalently, the sp^2 hybrid bonds will be converted to sp^3 hybrid to connect the atoms from substrate and Gr, which will then be responsible for the decrease of thermal conductivity. In another word, the excellent thermal conductivity of Gr layer can be strongly affected by the interfacial interactions. Therefore, we expect to see a Gr/3C-SiC nanocomposite with a lower thermal conductivity than that of pure SiC in practice. That is why in this simulation, the nanocomposite with two Gr layers performed higher thermal conductivity in comparison with three and four Gr layers. The work about thermal conductivity of Gr/3C-SiC nanocomposite laminate is not widely available in the literature, but some previous studies proved that the covalent bonds between Gr and SiC negatively affect the heat transfer [8; 18] and Papanikolaou [50] reported a very close range of thermal conductivity of 3C-SiC with a similar shape by molecular dynamics.

4. Conclusions

In this paper, we constructed a Gr/3C-SiC nanocomposite with covalent bonds connected in between via LAMMPS and evaluated its tribological, mechanical, and thermal properties with different model configurations using MD simulations. The main results were compared with the existing literature and was proved to be valid. Based on the discussions above, the following conclusions have been obtained.

(1) The composite laminate with covalent bonds connected between 3C-SiC as the matrix phase and Gr layers as the reinforcement phase is constructed. The covalent bonds between two phases play an important role in the overall properties of the Gr/3C-SiC nanocomposite.

(2) In the scratching model of the Gr/3C-SiC nanocomposite, the factors affecting the friction performances include the scratching depth, temperature, scratching speed and the number of Gr layers. During the scratching, stress concentrations take place in the laminate around the indenter and Gr layers. The closer the area in the workpiece to the indenter, the higher the temperature will be.

(3) It is found that the frictional force, normal force, and coefficient of friction increase with the scratching depth. At the same scratching depth, the laminate exhibited slightly lower frictional force and normal force than that of the perfect single crystal 3C-SiC, but the coefficient of friction of the laminate increased faster than that of the 3C-SiC when the scratching depth increases from 10 Å to 30 Å, though both materials had a very similar magnitude of coefficient of friction. The wear rate also increased with a larger scratching depth, and the laminate produced fewer worn atoms compared to pure SiC. The nanocomposite showed lowest wear rate with an appreciable coefficient of friction at the scratching depth of 10 Å.

(4) Under the range of scratching speed between 10 m/s and 80 m/s, the frictional force and normal force did not exhibit any obvious relationship with the scratching speed, which also brings the same result to coefficient of friction. The wear rate did not show a strong dependence on the scratching velocity, but apparently a faster scratching speed could produce wear debris more quickly. It was deduced that high velocity elevates the temperature of the material near the indenter faster, which may soften the material and degrade the mechanical properties. Therefore, a smaller scratching speed is preferrable for the friction material to maintain its performance. In the current study we found that 10 m/s was the optimal scratching speed.

(5) By varying the temperatures from 300 K, 500 K to 700 K, both the frictional force, normal force and the coefficient of friction decreased with the temperature. It is because a higher temperature can expedite the thermal softening effect and results in a higher wear rate. We found that a temperature of 300 K yielded the highest coefficient of friction and lowest wear rate in the present study.

(6) By changing the number of Gr layers from two to four, a reduction occurs in the frictional force, normal force and coefficient of friction as well. The addition of the Gr layers inserted in the SiC improved the wear resistance of the laminate and resulted in smaller wear rate. The model with three Gr showed a relatively high coefficient of friction and a relatively low wear rate.

(7) The effect of gap distance between the adjacent Gr layers (different amount of Gr layers in the 3C-SiC) was studied. The stacking of the Gr layers can improve both Young's modulus and UTS of the material compared to pure SiC. It has been found that Young's modulus and UTS increase with a reduction in the gap distance between the adjacent Gr layers (i.e. an increase in the Gr layer number). However, the formation and the growth of the damage from the interfaces between SiC and Gr layers during a tensile loading negatively affect the critical failure strain. We concluded that the model with five Gr layers stacked in 3C-SiC exhibited the best mechanical performance.

(8) The effect of different model lengths and number of graphene layers under the temperature of 300 K was evaluated. A longer model possesses higher thermal conductivity. The covalent bonded Gr with SiC provided channels for the phonons to pass, which reduced the number of phonons that passed through the laminate in the lateral direction and obstructed the heat transfer. This led to a lower thermal conductivity with more stacked Gr layers. As a consequence, the nanowire model with two Gr layers showed a higher thermal conductivity.

Based on the current result, in the future work, the more detailed influence mechanism of the interfaces in the laminate and the improvement on the thermal conductivity of the nanocomposite laminate will be studied. The new types of metal-free friction materials will be considered as well, such as particle-dispersed composite to obtain better material performance.

CRediT authorship contribution statement

Yizhan Zhang: Conceptualization, Methodology, Software, Data curation, Writing – original draft, Visualization, Investigation, Validation. **Kingsford Koranteng:** Writing – review & editing. **Yun-Bo Yi:** Writing – review & editing, Supervision, Project administration, Funding acquisition.

Declaration of Competing Interest

The authors declare that they have no known competing financial interests or personal relationships that could have appeared to influence the work reported in this paper.

Data availability

Data will be made available on request.

Acknowledgements

Support for this work, provided by the National Science Foundation under Contract (No. 1928876), is gratefully acknowledged.

Appendix A. Supplementary data

Supplementary data to this article can be found online at https://doi.org/10.1016/j.commatsci.2022.111973.

References

[1] W. Zhang, Tribology of SiC ceramics under lubrication: Features, developments, and perspectives, Curr. Opin. Solid State Mater. Sci. 26 (4) (2022) 101000.

[2] Y. Zhou, K. Hirao, Y. Yamauchi, S. Kanzaki, Tribological Properties of Silicon Carbide and Silicon Carbide-Graphite Composite Ceramics in Sliding Contact, J. Am. Ceram. Soc. 86 (2003) 991–1002, https://doi.org/10.1111/j.1151-2916.2003.tb03407.x.

[3] X. Liu, X. Zhou, F. Kuang, H. Zuo, J. Huang, Mechanical and Tribological Properties of Nitrile Rubber Reinforced by Nano–SiO2: Molecular Dynamics Simulation, Tribol. Lett. 69 (2) (2021), https://doi.org/10.1007/s11249-021-01427-9.

[4] D. Berman, A. Erdemir, A.V. Zinovev, A.V. Sumant, Nanoscale friction properties of graphene and graphene oxide, Diam. Relat. Mater. 54 (2015) 91–96, https://doi.org/10.1016/j.diamond.2014.10.012.

[5] D.G. Papageorgiou, L.A. Kinloch, R.J. Young, Mechanical properties of graphene and graphene-based nanocomposites, Prog. Mater. Sci. 90 (2017) 75–127, https://doi.org/10.1016/j.pmatsci.2017.07.004.

[6] E. Pop, V. Varshney, A.K. Roy, Thermal properties of graphene: Fundamentals and applications, MRS Bull. 37 (2012) 1273–1281, https://doi.org/10.1557/mrs.2012.203.

[7] N. Izzaty, H.Y. Sastra, Ilyas, Ilyas, The Implementation of Graphene Composites for Automotive: An Industrial Perspective, IOP Conf. Ser. Mater. Sci. Eng. 536 (1) (2019) 012133.

[8] Y. Zhu, H. Ji, H.M. Cheng, R.S. Ruoff, Mass production and industrial applications of graphene materials, Natl. Sci. Rev. 5 (2018) 90–101, https://doi.org/10.1093/nsr/nwx055.

[9] J.M. Zhan, X.H. Yao, W.H. Li, X.Q. Zhang, Tensile mechanical properties study of SiC/graphene composites based on molecular dynamics, Comput. Mater. Sci. 131 (2017) 266–274, https://doi.org/10.1016/j.commatsci.2017.02.006.

[10] M. Barfmal, A. Montazeri, MD-based design of SiC/graphene nanocomposites towards better mechanical performance, Ceram. Int. 43 (2017) 17167–17173, https://doi.org/10.1016/j.ceramint.2017.09.140.

[11] Y. Kumar, S. Sahoo, A.K. Chakraborty, Mechanical properties of graphene, defective graphene, multilayer graphene and SiC-graphene composites: A molecular dynamics study, Phys. Rev. B Condens. Matter 620 (2021), 413250, https://doi.org/10.1016/j.physb.2021.413250.

[12] M. Li, J. Zhang, X. Hu, Y. Yue, Thermal transport across graphene/SiC interface: effects of atomic bond and crystallinity of substrate, Appl. Phys. A Mater. Sci. Process. 119 (2015) 415–424, https://doi.org/10.1007/s00339-015-9066-7.

[13] B. Román-Manso, Y. Chevillotte, M.I. Osendi, M. Belmonte, P. Miranzo, Thermal conductivity of silicon carbide composites with highly oriented graphene nanoplatelets, J. Eur. Cream. Soc. 36 (16) (2016) 3987–3993.

[14] A. Rahman et al., Graphene Reinforced Silicon Carbide Nanocomposites: Processing and Properties, in: G. Tandon, Composite, Hybrid, and Multifunctional Materials, Volume 4, Springer, Cham, 2014, pp. 165-176. https://doi.org/10.1007/978-3-319-06992-0_21.

[15] J. Llorente, B. Román-Manso, P. Miranzo, M. Belmonte, Tribological performance under dry sliding conditions of graphene/silicon carbide composites, J. Eur. Ceram. Soc. 36 (2016) 429–435, https://doi.org/10.1016/j.jeurceramsoc.2015.09.040.

[16] L. Zhao, J. Zhang, J. Pfetzing, M. Alam, A. Hartmaier, Depth-sensing ductile and brittle deformation in 3C-SiC under Berkovich nanoindentation, Mater. Des. 197 (2021) 109223.

[17] Y. Li, S. Wang, Q. Wang, A molecular dynamics simulation study on enhancement of mechanical and tribological properties of polymer composites by introduction of graphene, Carbon 111 (2017) 538–545, https://doi.org/10.1016/j.carbon.2016.10.039.

[18] Z.X. Guo, J.W. Ding, X.G. Gong, Substrate effects on the thermal conductivity of epitaxial graphene nanoribbons, Phys. Rev. B Condens. Mater. Phys. 85 (2012), https://doi.org/10.1103/PhysRevB.85.235429.

[19] H. Zhuang, B. Yang, S. Heuser, N. Huang, H. Fu, X. Jiang, Graphene/3C-SiC Hybrid Nanolaminate, ACS Appl. Mater. Interfaces 7 (51) (2015) 28508–28517.

[20] J.-L. Chen, P.-Y. Ji, C.-G. Jin, L.-J. Zhuge, X.-M. Wu, Synthesis of SiC/ graphene nanosheet composites by helicon wave plasma, Chin. Phys. B 30 (7) (2021) 075201.

[21] T. Filleter, R. Bennewitz, Structural and frictional properties of graphene films on SiC(0001) studied by atomic force microscopy, Phys. Rev. B Condens. Matter 81 (2010), https://doi.org/10.1103/PhysRevB.81.155412.

[22] A. Masud, C.L. Tham, in: Computational Mechanics in Structural Engineering, Elsevier, 1999, pp. 295–307.

[23] E.F. Sukur, G. Onal, Thermal Conductivity of Graphene Laminate, Wear 460–461 (2020), 203481, https://doi.org/10.1016/j.wear.2020.203481.

[24] B. Mortazai, T. Rabczuk, Multiscale modeling of heat conduction in graphene laminates, Carbon 85 (2015) 1–7, https://doi.org/10.1016/j.carbon.2014.12.046.

[25] Z. Yin, P. Zhu, B. Li, Study of Nanoscale Wear of SiC/Al Nanocomposites Using Molecular Dynamics Simulations, Tribol. Lett. 69 (2021), https://doi.org/10.1007/s11249-021-01414-0.

[26] J. Tersoff, Modeling solid-state chemistry: Interatomic potentials for multicomponent systems, Phys. Rev. B 39 (8) (1989) 5566–5568.

[27] S.J. Stuart, A.B. Alan, J.A. Harrison, A reactive potential for hydrocarbons with intermolecular interactions, J. Chem. Phys. 2000 (2000) 6472–6486, https://doi.org/10.1063/1.481208.

[28] C. Qian, B. McLean, D. Hedman, F. Ding, A comprehensive assessment of empirical potentials for carbon materials, APL Mater. 9 (2021) 61102, https://doi.org/10.1063/5.0052870.

[29] T.H. Fang, C.I. Weng, J.G. Chang, Molecular dynamics simulation of nano-lithography process using atomic force microscopy, Surf. Sci. 501 (2002) 138–147, https://doi.org/10.1016/S0039-6028(01)01938-0.

[30] A.P. Thompson, H.M. Aktulga, R. Berger, D.S. Bolintineanu, W.M. Brown, P. S. Crozier, P.J. in 't Veld, A. Kohlmeyer, S.G. Moore, T.D. Nguyen, R. Shan, M. J. Stevens, J. Tranchida, C. Trott, S.J. Plimpton, LAMMPS - a flexible simulation tool for particle-based materials modeling at the atomic, meso, and continuum scales, Comput. Phys. Commun. 271 (2022) 108171.

[31] A. Stukowski, Visualization and analysis of atomistic simulation data with OVITO–the Open Visualization Tool, Model. Simul. Mater. Sci. Eng., 18 (2010), 015012-015012. https://doi.org/10.1088/0965-0393/18/1/015012.

[32] L. Verlet, Computer "Experiments" on Classical Fluids. I. Thermodynamical Properties of Lennard-Jones Molecules, Phys. Rev. 159 (1967) 98–103, https://doi.org/10.1103/PhysRev.159.98.

[33] M.S. Green, Markoff Random Processes and the Statistical Mechanics of Time-Dependent Phenomena. II. Irreversible Processes in Fluids, J. Chem. Phys. 22 (1954) 398–413, https://doi.org/10.1063/1.1740082.

[34] R. Kubo, Statistical-Mechanical Theory of Irreversible Processes. I. General Theory and Simple Applications to Magnetic and Conduction Problems, J. Phys. Soc. Jpn. 12 (1957) 570–586, https://doi.org/10.1143/JPSJ.12.570.

[35] Y. Tang, Z. Zhang, L. Li, J. Guo, P. Yang, Thermal transport enhancement resolution for graphene/Si and graphene/SiC interfaces, Int. J. Therm. Sci. 171 (2022) 107231.

[36] J.P. Gao, et al., Frictional Forces and Amontons' Law: From the Molecular to the Macroscopic Scale, J. Phys. Chem. B 108 (2004) 3410–3425, https://doi.org/10.1021/jp036362l.

[37] L. Wu, X. Sun, F. Gong, J. Luo, C. Yin, Z. Sun, R. Xiao, Enhanced Thermal Transport Properties of Graphene/SiC Heterostructures on Nuclear Reactor Cladding Material: A Molecular Dynamics Insight, Nanomater. 12 (6) (2022) 894.

[38] M. Morita, Y. Oya, N. Kato, K. Mori, J. Koyanagi, Effect of Electrostatic Interactions on the Interfacial Energy between Thermoplastic Polymers and Graphene Oxide: A Molecular Dynamics Study, Polymers 14 (13) (2022) 2579.

[39] K.-S. Kim, H.-J. Lee, C. Lee, S.-K. Lee, H. Jang, J.-H. Ahn, J.-H. Kim, H.-J. Lee, Chemical Vapor Deposition-Grown Graphene: The Thinnest Solid Lubricant, ACS nano 5 (6) (2011) 5107–5114.

[40] J.F. Archard, Contact and Rubbing of Flat Surface, J. Appl. Phys. 24 (1953) 981–988, https://doi.org/10.1063/1.1721448.

[41] A. Okabe, B. Boots, K. Sugihara, S.N. Chiu, Spatial Tessellations: Concepts and Applications of Voronoi Diagrams, Second ed., John Wiley & Sons, New York, 2000.

[42] E.A. Lazar, J. Lu, C.H. Rycroft, Voronoi cell analysis: The shapes of particle systems, Am. J. Phys. 90 (2022) 469–480, https://doi.org/10.1119/5.0087591.

[43] M. Kumar, J. Bijwe, Role of different metallic fillers in non-asbestos organic (NAO) friction composites for controlling sensitivity of coefficient of friction to load and speed, Tribol. Int. 43 (2010) 965–974, https://doi.org/10.1016/j.triboint.2009.12.062.

[44] D. Pan, H. Wang, L. Sun, K. Zhu, X. Hao, Effect of Temperature on Fe–Polytetrafluoroethylene Friction Coefficient Using Molecular Dynamics Simulation, Tribol. Trans. 65 (4) (2022) 705–715.

[45] J.O. Chung, S.R. Go, H.B. Choi, T.K. Son, Temperature dependence of friction coefficient and transfer film formation in organic friction materials containing different abrasive components, Ind. Lubr. Tribol. 72 (2020) 483–489, https://doi.org/10.1108/ILT-10-2019-0427.

[46] F. Javanshour, K.R. Ramakrishnan, R.K. Layek, P. Laurikainen, A. Prapavesis, M. Kanerva, P. Kallio, A.W. Van Vuure, E. Sarlin, Effect of graphene oxide surface treatment on the interfacial adhesion and the tensile performance of flax epoxy composites, Compos. Part A Appl. Sci. Manuf. 142 (2021) 106270.

[47] J. Koyanagi, N. Takase, K. Mori, T. Sakai, Molecular dynamics simulation for the quantitative prediction of experimental tensile strength of a polymer material, JCOMC 2 (2020), 100041, https://doi.org/10.1016/j.jcomc.2020.100041.

[48] B. Xu, D. Chen, H. Yang, R. Luo, L. Wang, Z. Chen, M. Li, Q. Yuan, Y. Hua, J. Zhou, Y. He, Y. Huo, T. Liu, Effect of strain rate on the tensile properties of mini-SiC/SiC composites, Ceram. Int. 48 (2) (2022) 2092–2096.

[49] M. Mathias, M. Günter, J. Gemmer, Fourier's Law from Schrödinger Dynamics, Phys. Rev. Lett., 95 (2005), 1860602.1-180602.4. https://doi.org/10.1103/PhysRevLett.95.180602.

[50] N. Papanikolaou, Lattice thermal conductivity of SiC nanowires, J. Phys.: Condens. Matter 20 (13) (2008) 135201.